

A “vertically Lagrangian” finite-volume dynamical core for global models

27th February 2004

Submitted to Monthly Weather Review, revised

by

Shian-Jiann Lin

NOAA/Geophysical Fluid Dynamics Laboratory, Princeton University

Princeton, NJ 08544

*Corresponding author address: NOAA/Geophysical Fluid Dynamics Laboratory, Forresteral
Campus, Princeton University, Princeton, NJ 08544-0308. E-mail: Shian-Jiann.Lin@noaa.gov

Abstract

A finite-volume dynamical core with a terrain-following Lagrangian control-volume discretization is described. The vertically Lagrangian discretization reduces the dimensionality of the physical problem from three to two with the resulting dynamical system closely resembling that of the shallow water system. The 2D horizontal-to-Lagrangian-surface transport and dynamical processes are then discretized using the genuinely conservative flux-form semi-Lagrangian algorithm. Time marching is split-explicit, with large-time-step for scalar transport, and small fractional step for the Lagrangian dynamics, which permits the accurate propagation of fast waves. A mass, momentum, and total energy conserving algorithm is developed for remapping the state variables periodically from the floating Lagrangian control-volume to an Eulerian terrain-following coordinate for dealing with “physical parameterizations” and to prevent severe distortion of the Lagrangian surfaces. Deterministic baroclinic wave growth tests and long-term integrations using the Held-Suarez forcing are presented. Impact of the monotonicity constraint is discussed.

1. Introduction This paper describes the finite-volume dynamical core for global models that was initially developed at the NASA Goddard Space Flight Center. The applications of the finite-volume algorithms for global modeling at NASA Goddard Space Flight Center (GSFC) started in the late 80s and early 90s with focus on the transport process of chemistry constituents (*e.g.*, Rood 1987; Allen *et al.* 1991 and 1996) and water vapor (Lin *et al.* 1994). These algorithms were derived and evolved from the modern 1D finite-volume algorithms pioneered by van Leer (1977) and Colella and Woodward (1984), which were originally designed for resolving sharp gradients and discontinuities in astrophysics and aerospace engineering applications.

In addition to the effort at NASA/GSFC, finite-volume schemes have also been developed or applied elsewhere for modeling geophysical flows (*e.g.*, Carpenter *et al.* 1991; Machenhauer and Olk 1995; Thuburn 1996). The challenge to us was to develop computationally competitive and physically based algorithms suitable for global modeling of both weather and climate systems. There exists rich body of literature on high performance finite-volume schemes designed for other disciplines (*e.g.*, Roe 1981; Colella and Woodward 1984; Woodward and Colella 1984; Shu and Osher 1988; Harten 1989; Huynh 1996; Leveque 2002). However, the large-scale atmospheric flow is highly stratified in the direction of gravitation, and as an excellent approximation, hydrostatic. As such, the standard “Riemann solver” developed for other disciplines would not be efficient nor directly applicable. Furthermore, the directional splitting needed for applying the above-mentioned 1D algorithms would produce unacceptably large errors near the poles where the splitting errors are greatly amplified by the convergence of the meridians (Lin and Rood 1996).

A milestone toward the goal of developing a finite-volume dynamical core was achieved in early 1994¹ with the development of the multi-dimensional “Flux-Form Semi-Lagrangian Transport” scheme (FFSL, Lin and Rood 1996; referred to as LR96 hereafter). Building on the existing 1D finite-volume schemes, the FFSL algorithm extended those schemes to mul-

¹The multi-dimensional Flux-Form Transport Algorithm was first presented in 1994 at the 4th Workshop on the Solutions of Partial Differential Equations on the Sphere and later published in 1996.

tidimensions and thereby eliminated the need for directional splitting. Equally important, the so-called “Pole-Courant number problem” is solved, via the physical consideration of the contribution to fluxes from upstream volumes as far away as the Courant number indicated. The resulting multi-dimensional scheme is *oscillation free* (with the optional monotonicity constraint), mass conserving, and stable for Courant number greater than one in the longitudinal direction, which made the scheme competitive for the intended application on the sphere. The FFSL algorithm has since been adopted in several atmospheric chemistry transport models (*e.g.*, Chin et al. 2000 and Rotman *et al.* 2001).

Another milestone towards the goal of building the finite-volume dynamical core was reached with the adaptation of the FFSL algorithm to the shallow water dynamical framework (Lin and Rood 1997; referred to as LR97 hereafter). To achieve the goal of consistent transport of the mass, the absolute vorticity, and hence, the potential vorticity, a two-grid two-step “reversed engineering approach” was developed. It has the advantage of the Z grid (Randall 1994) without its computational expense of solving an elliptic equation. The time discretization for treating the gravity waves on both grids is the explicit “forward-backward” scheme, which is conditionally stable with the *forward-in-time* nature of the FFSL transport algorithm. The allowable size of the time step, for example, for a T42-like resolution (about 2.8°) is 600 seconds, which is about half of what can be used by the semi-implicit Eulerian spectral model. This not-so-small time step made the fully explicit shallow water algorithm computationally competitive with the spectral and finite difference methods (*e.g.*, Bourke 1974; Arakawa and Lamb 1981; Ringler *et al.* 2000).

The final piece needed for the completion of the finite-volume dynamical core was developed after the discovery of a simple finite-volume integration method for computing the pressure gradient in general terrain-following coordinates (Lin 1997 and 1998; referred to as L97 and L98 hereafter). It is well known that the standard mathematical transformation of the pressure gradient term in terrain-following coordinates results in two large-in-magnitude terms with opposite sign. A straightforward application of numerical techniques (*e.g.*, center

differencing) to these two terms would typically produce large errors. The finite-volume integration scheme of L97 avoids the mathematical transformation by integrating around the arbitrarily shaped finite-volume to accurately determine the pressure gradient forcing so as to maintain the physical consistency for the finite volume under consideration.

The finite-volume dynamical core developed in L97 utilized a sigma vertical coordinate, which requires a 3D transport algorithm. Applying the methodology of LR96, a fully 3D FFSL algorithm would require 6 permutations of 1D operators, instead of 2 as in 2D. To reduce the computational cost, a simplification was made in L97, with some loss in accuracy, to reduce the operator permutations from 6 to 3, and even down to 2 (*i.e.*, no cross terms associated with vertical transport, as was done in LR96). This computationally motivated simplification is no longer needed after the introduction of the Lagrangian control-volume vertical discretization (Lin and Rood 1998 and Lin and Rood 1999) as the dimensionality of the physical problem is essentially reduced from three to two, as viewed from the Lagrangian control-volume perspective.

For reference purpose, the full governing equations for the atmosphere under the hydrostatic approximation are provided in appendix-A using a general vertical coordinate. Upon the introduction of the Lagrangian control-volume vertical discretization, all prognostic equations are reduced to 2D, in the sense that they are vertically decoupled. The discretization of the 2D horizontal transport process is described in section 2. The complete dynamical system with the Lagrangian control-volume vertical discretization is described in section 3. A mass, momentum, and total energy conserving remapping algorithm is described in section 4. We present in section 5, the deterministic baroclinic wave growth tests and long term integrations using the Held-Suarez forcing (Held and Suarez 1994). Concluding remarks are given in section 6.

2. Discretization of the horizontal transport process We shall follow the equations and notations in Appendix-A. Since the vertical transport terms vanish with the Lagrangian

control-volume vertical discretization, we present here only the 2D forms of the FFSL algorithm for the transport of density and mixing ratio like quantities. the conservation law for the pseudo-density [Eq. (41)] reduces to

$$\frac{\partial}{\partial t}\pi + \frac{1}{A\cos\theta} \left[\frac{\partial}{\partial\lambda}(u\pi) + \frac{\partial}{\partial\theta}(v\pi\cos\theta) \right] = 0 \quad (1)$$

Integrating Eq. (1) analytically in time (for one time step Δt) and around the finite-volume, the above conservation law becomes

$$\tilde{\pi}^{n+1} = \tilde{\pi}^n - \frac{1}{A^2\Delta\theta\Delta\lambda\cos\theta} \int_t^{t+\Delta t} \left[\oint \pi(\tau; \lambda, \theta) \vec{V} \cdot \vec{n} dl \right] d\tau, \quad (2)$$

where $\vec{V}(t; \lambda, \theta) = (U, V)$, dl is the infinitesimal element along the volume edges, \vec{n} is the corresponding outward normal vector, $\tilde{\pi}$ is the finite-volume representation of π , and the contour integral is taken along the edges of the finite-volume centered at (λ, θ) .

$$\tilde{\pi}(t) \equiv \frac{1}{A^2\Delta\theta\Delta\lambda\cos\theta} \int_{\lambda-\Delta\lambda/2}^{\lambda+\Delta\lambda/2} \int_{\theta-\Delta\theta/2}^{\theta+\Delta\theta/2} \pi(t; \lambda, \theta) A^2\cos\theta d\theta d\lambda \quad (3)$$

Equation (2) is still *exact*. To carry out the contour integral, certain approximations must be made. LR96 effectively decomposed the flux integral using two orthogonal 1D flux-form transport operators. Introducing the difference and average operators:

$$\delta_x q = q\left(x + \frac{\Delta x}{2}\right) - q\left(x - \frac{\Delta x}{2}\right), \quad \bar{q}^x = \frac{1}{2} \left[q\left(x + \frac{\Delta x}{2}\right) + q\left(x - \frac{\Delta x}{2}\right) \right]$$

and assuming (u^*, v^*) is the time-averaged (from time t to time $t + \Delta t$) \vec{V} on the C-grid (*e.g.*, Fig. 1 in LR96), the 1-D flux-form transport operator F in the λ -direction is

$$F(u^*, \Delta t, \tilde{\pi}) = -\frac{1}{A\Delta\lambda\cos\theta} \delta_\lambda \left[\int_t^{t+\Delta t} \pi U d\tau \right] = -\frac{\Delta t}{A\Delta\lambda\cos\theta} \delta_\lambda [\chi(u^*, \Delta t; \pi)] \quad (4)$$

$$\chi(u^*, \Delta t; \pi) = \frac{1}{\Delta t} \int_t^{t+\Delta t} \pi U d\tau \equiv u^* \pi^*(u^*, \Delta t, \tilde{\pi}) \quad (5)$$

$$\pi^*(u^*, \Delta t; \tilde{\pi}) \approx \frac{1}{\Delta t} \int_t^{t+\Delta t} \pi d\tau \quad (6)$$

where χ is the time-accumulated (from t to $t+\Delta t$) mass flux across the cell wall, and π^* can be interpreted as a time-mean (from time t to time $t+\Delta t$) pseudo-density value of all material that passed through the cell edge. To be exact, the time integration in Eq. (6) should be carried out along the *backward-in-time* trajectory of the cell edge position from $t = t + \Delta t$ back to time t . The essence of the 1D finite-volume algorithm is to construct, based on the given initial cell-mean values of $\tilde{\pi}$, an approximated subgrid distribution of the true π field, to enable an analytic integration of Eq. (6). Assuming there is no error in obtaining the time-mean wind (u^*), the only error produced by the 1D transport scheme would be solely due to the approximation to the true distribution of π using the assumed subgrid distribution. From this perspective, it can be said that the 1D finite-volume transport algorithm combined the space-time discretization in the approximation of the time-mean cell-edge value π^* . The physically correct way of approximating the integral in Eq. (6) must be “upwind”, in the sense that it is integrated along the backward trajectory of the cell edges. A center difference approximation to Eq. (6) would be physically incorrect, and consequently numerically unstable without additional numerical damping.

Central to the accuracy and computational efficiency of the finite-volume algorithms is the degrees of freedom that describe the subgrid distribution. The first order upwind scheme has zero degree of freedom within the volume as it is assumed that the subgrid distribution is piecewise constant having the same value everywhere within the cell as the given volume-mean. The second order finite-volume scheme assumes a piece-wise linear subgrid distribution, which allows one degree of freedom for the specification of the “slope” (or equivalently, the “*mismatch*” as defined by Lin et al. 1994). The Piecewise Parabolic Method

(PPM) has two degrees of freedom in the construction of the second order polynomial within the volume, and as a result, the accuracy is significantly enhanced. The PPM strikes a good balance between computational efficiency and accuracy. To further improve its accuracy, a modified PPM is presented in appendix-B.

While the PPM possesses all the desirable attributes (mass conserving, monotonicity preserving, and high-order accuracy) in 1D, a solution must be found to avoid the directional splitting for modeling the multidimensional dynamics and the transport processes. For 2D problems, the first step towards reducing the splitting error is to apply the two orthogonal 1D flux-form operators in a symmetric way. After the directional symmetry is achieved (by averaging), the “inner operators” are then replaced with corresponding advective-form operators. A consistent advective-form operator (f) in the λ -direction can be derived from its flux-form counterpart (F) as follows.

$$f(u^*, \Delta t, \tilde{\pi}) = F(u^*, \Delta t, \tilde{\pi}) - \tilde{\pi} F(u^*, \Delta t, \tilde{\pi} \equiv 1) = F(u^*, \Delta t, \tilde{\pi}) + \tilde{\pi} C_{def}^\lambda \quad (7)$$

$$C_{def}^\lambda = \frac{\Delta t \delta_\lambda u^*}{A \Delta \lambda \cos \theta} \quad (8)$$

where C_{def}^λ is a dimensionless number indicating the degree of the flow deformation in the λ -direction. The above derivation of f is different from LR96’s approach, which adopted the traditional 1D advective-form semi-Lagrangian scheme. The advantage of using Eq. (7) is that computations of winds at cell centers are avoided.

Analogously, 1D flux-form transport operator G in the latitudinal (θ) direction is derived as follows.

$$G(v^*, \Delta t, \tilde{\pi}) = -\frac{1}{A \Delta \theta \cos \theta} \delta_\theta \left[\int_t^{t+\Delta t} \pi V \cos \theta d\tau \right] = -\frac{\Delta t}{A \Delta \theta \cos \theta} \delta_\theta [v^* \cos \theta \pi^*] \quad (9)$$

and likewise the advective-form operator is

$$g(v^*, \Delta t, \tilde{\pi}) = G(v^*, \Delta t, \tilde{\pi}) + \tilde{\pi} C_{def}^\theta \quad (10)$$

where

$$C_{def}^\theta = \frac{\Delta t \delta_\theta [v^* \cos \theta]}{A \Delta \theta \cos \theta} \quad (11)$$

Introducing the following short hand notations:

$$()^\theta = ()^n + \frac{1}{2} g[v^*, \Delta t, ()^n] \quad (12)$$

$$()^\lambda = ()^n + \frac{1}{2} f[u^*, \Delta t, ()^n] \quad (13)$$

the 2D transport algorithm on the sphere can then be written as

$$\tilde{\pi}^{n+1} = \tilde{\pi}^n + F[u^*, \Delta t, \tilde{\pi}^\theta] + G[v^*, \Delta t, \tilde{\pi}^\lambda] \quad (14)$$

Using explicitly the mass fluxes (χ, Y) , Eq. (14) is rewritten as

$$\tilde{\pi}^{n+1} = \tilde{\pi}^n - \frac{\Delta t}{A \cos \theta} \left\{ \frac{1}{\Delta \lambda} \delta_\lambda [\chi(u^*, \Delta t; \tilde{\pi}^\theta)] + \frac{1}{\Delta \theta} \delta_\theta [\cos \theta Y(v^*, \Delta t; \tilde{\pi}^\lambda)] \right\} \quad (15)$$

where Y , the mass flux in the meridional direction, is defined in a similar fashion as χ . It can be verified that in the special case of constant density flow, $\tilde{\pi} = \text{constant}$, the above equation degenerates to the discrete representation of the *incompressibility condition* of the wind field (u^*, v^*)

$$\frac{1}{\Delta \lambda} \delta_\lambda u^* + \frac{1}{\Delta \theta} \delta_\theta (v^* \cos \theta) = 0 \quad (16)$$

The fulfillment of the above *incompressibility condition* for constant density flows is

crucial to the accuracy of the 2D flux-form formulation. For transport of mixing ratio like quantities (\tilde{q}) the mass fluxes (χ, Y) as defined previously should be used as follows.

$$\tilde{q}^{n+1} = \frac{1}{\tilde{\pi}^{n+1}} [\tilde{\pi}^n \tilde{q}^n + F(\chi, \Delta t, \tilde{q}^\theta) + G(Y, \Delta t, \tilde{q}^\lambda)] \quad (17)$$

The above form of the tracer transport equation consistently degenerates to Eq 15 if $\tilde{q} = \text{constant}$, which is another important condition for a flux-form transport algorithm to be able to avoid generation of artificial gradients and to maintain mass conservation.

3. The vertically Lagrangian control-volume discretization

The very idea of using Lagrangian vertical coordinate for formulating governing equations for the atmosphere is not new. Starr (1945) is the first to formulate the governing equations using the Lagrangian coordinate approach. Starr did not make use of the Lagrangian control-volume concept for discretization nor did he present a solution to the problem of computing the pressure gradient terms. In the *finite-volume discretization*, the Lagrangian surfaces are treated as the bounding material surfaces of the Lagrangian control-volumes within which the finite-volume algorithms developed in LR96, LR97, and L97 will be directly applied.

To use a vertical Lagrangian coordinate system, one should first address the issue of whether it is an inertial coordinate or not. For hydrostatic flows, it is. This is because both sides of the vertical momentum equation vanish under the hydrostatic assumption. Realizing that the earth's surface, for modeling purpose, is a material surface, one can then construct a terrain-following *Lagrangian* control-volume coordinate using the usual terrain-following *Eulerian* coordinate as the starting point. The basic idea is to start the time integration from the chosen terrain-following Eulerian coordinate (*e.g.*, pure σ or hybrid σ - p), *treating all initial coordinate surfaces as material surfaces*, the finite-volumes bounded by two coordinate surfaces, *i.e.*, the Lagrangian control-volumes, are free vertically, to float, compress, or expand with the flow as dictated by the hydrostatic dynamics.

By choosing an *imaginary* conservative tracer ζ that is a monotonic function of height

and constant on the initial coordinate surfaces, the 3D equations written for the general vertical coordinate in Appendix-A can be reduced to 2D forms. After factoring out the constant $\delta\zeta$, Eq. (41) in appendix-A, the conservation law for the pseudo-density ($\pi = \frac{\delta p}{\delta\zeta}$), becomes

$$\frac{\partial}{\partial t}\delta p + \frac{1}{A\cos\theta} \left[\frac{\partial}{\partial\lambda}(u\delta p) + \frac{\partial}{\partial\theta}(v\delta p \cos\theta) \right] = 0 \quad (18)$$

where the operator δ represents the vertical difference between the two neighboring Lagrangian surfaces that bound the finite control-volume. From the hydrostatic balance, Eq. (39), the pressure thickness δp of that control-volume is proportional to the total mass, *i.e.*, $\delta p = -\rho g \delta z$. Therefore, it can be said that the Lagrangian control-volume vertical discretization has the hydrostatic balance built-in.

Similarly, Eq. (42), the mass conservation law for all tracer species is

$$\frac{\partial}{\partial t}(q\delta p) + \frac{1}{A\cos\theta} \left[\frac{\partial}{\partial\lambda}(uq\delta p) + \frac{\partial}{\partial\theta}(vq\delta p \cos\theta) \right] = 0, \quad (19)$$

the thermodynamic equation, Eq. (43), becomes

$$\frac{\partial}{\partial t}(\Theta\delta p) + \frac{1}{A\cos\theta} \left[\frac{\partial}{\partial\lambda}(u\Theta\delta p) + \frac{\partial}{\partial\theta}(v\Theta\delta p \cos\theta) \right] = 0, \quad (20)$$

and (44) and (45), the momentum equations, are reduced to

$$\frac{\partial}{\partial t}u = \Omega v - \frac{1}{A\cos\theta} \left[\frac{\partial}{\partial\lambda}(\kappa + \phi - \nu D) + \frac{1}{\rho} \frac{\partial}{\partial\lambda}p \right] \quad (21)$$

$$\frac{\partial}{\partial t}v = -\Omega u - \frac{1}{A} \left[\frac{\partial}{\partial\theta}(\kappa + \phi - \nu D) + \frac{1}{\rho} \frac{\partial}{\partial\theta}p \right] \quad (22)$$

Given the prescribed pressure at the model top P_∞ , the position of each Lagrangian surface P_l (horizontal subscripts omitted) is determined in terms of the hydrostatic pressure as follows.

$$P_l = P_\infty + \sum_{k=1}^l \delta P_k, \quad (\text{for } l = 1, 2, 3, \dots, N) \quad (23)$$

where the subscript l is the vertical index ranging from 1 at the lower bounding Lagrangian surface of the first (the highest) layer to N at the Earth's surface. There are $N+1$ Lagrangian surfaces to define N Lagrangian layers [here we use “layer” interchangeably with “control-volume”]. The surface pressure, which is the pressure at the lowest Lagrangian surface, is computed as P_N by Eq. (23).

With the exception of the pressure-gradient terms and the addition of a thermodynamic equation, the above 2D Lagrangian dynamical system is the same as the shallow water system described in LR97. The conservation law for the depth of fluid h in the shallow water system of LR97 is replaced by Eq. (18) for the pressure thickness δp . The ideal gas law, the mass conservation law for air mass, the conservation law for the potential temperature, together with the modified momentum equations Eq. (21) and (22) close the 2D Lagrangian dynamical system, which are vertically coupled only by the discretized hydrostatic relation.

The time marching procedure for the 2D Lagrangian dynamics follows closely that of the shallow water dynamics described in LR97. For computational efficiency, we take advantage of the stability of the FFSL transport algorithm by using a much larger time step (Δt) for the transport of all tracer species (including water vapor). The Lagrangian dynamics uses a relatively small time step, $\Delta \tau = \Delta t/m$, where m is the number of the sub-cycling needed to stabilize the fastest wave. We describe here a time-split procedure for the *prognostic variables* $[\delta p, \Theta, u, v; q]$ on the D-grid. Discretization on the C-grid for obtaining the *diagnostic variables* (u^*, v^*) , is analogous to that of the D-grid (see LR97).

Introducing the following short hand notations

$$(\cdot)_i^\theta = (\cdot)^{n+\frac{i-1}{m}} + \frac{1}{2}g[v_i^*, \Delta \tau, (\cdot)^{n+\frac{i-1}{m}}], \quad (\cdot)_i^\lambda = (\cdot)^{n+\frac{i-1}{m}} + \frac{1}{2}f[u_i^*, \Delta \tau, (\cdot)^{n+\frac{i-1}{m}}]$$

and applying Eq. (15), the update of “pressure thickness” δp , using the fractional time step

$\Delta\tau = \Delta t/m$, can be written for fractional step $i = 1, \dots, m$

$$\delta p^{n+\frac{i}{m}} = \delta p^{n+\frac{i-1}{m}} - \frac{\Delta\tau}{A\cos\theta} \left\{ \frac{1}{\Delta\lambda} \delta_\lambda [x_i^*(u_i^*, \Delta\tau; \delta p_i^\theta)] + \frac{1}{\Delta\theta} \delta_\theta [\cos\theta y_i^*(v_i^*, \Delta\tau; \delta p_i^\lambda)] \right\} \quad (24)$$

where $[x_i^*, y_i^*]$ are the air mass fluxes, which are then used as input to Eq. (17) for transport of the potential temperature Θ .

$$\Theta^{n+\frac{i}{m}} = \frac{1}{\delta p^{n+\frac{i}{m}}} \left[\delta p^{n+\frac{i-1}{m}} \Theta^{n+\frac{i-1}{m}} + F(x_i^*, \Delta\tau; \Theta_i^\theta) + G(y_i^*, \Delta\tau; \Theta_i^\lambda) \right] \quad (25)$$

With the exception of the pressure gradient terms, the discretization of the momentum equations are the same as those in the shallow water system (LR97).

$$u^{n+\frac{i}{m}} = u^{n+\frac{i-1}{m}} + \Delta\tau \left[y_i^*(v_i^*, \Delta\tau; \Omega^\lambda) - \frac{1}{A\Delta\lambda\cos\theta} \delta_\lambda(\kappa^* - \nu D^*) + \widehat{P}_\lambda \right] \quad (26)$$

$$v^{n+\frac{i}{m}} = v^{n+\frac{i-1}{m}} - \Delta\tau \left[x_i^*(u_i^*, \Delta\tau; \Omega^\theta) + \frac{1}{A\Delta\theta} \delta_\theta(\kappa^* - \nu D^*) - \widehat{P}_\theta \right] \quad (27)$$

where κ^* and D^* , both defined at the corners of the cell (grid), are discretized as

$$\kappa^* = \frac{1}{2} \left[x_i^*(\overline{u_i^*}^\theta, \Delta\tau; u^{n+\frac{i-1}{m}}) + y_i^*(\overline{v_i^*}^\lambda, \Delta\tau; v^{n+\frac{i-1}{m}}) \right]$$

$$D^* = \frac{1}{A\cos\theta} \left[\frac{1}{\Delta\lambda} \delta_\lambda u^{n+\frac{i-1}{m}} + \frac{1}{\Delta\theta} \delta_\theta \left(v^{n+\frac{i-1}{m}} \cos\theta \right) \right]$$

The finite-volume mean pressure-gradient terms in Eq. (26) and Eq. (27) are computed as:

$$\widehat{P}_\lambda = \frac{\oint_{\Pi=\lambda} \phi d\Pi}{A\cos\theta \oint_{\Pi=\lambda} \Pi d\lambda}, \quad \widehat{P}_\theta = \frac{\oint_{\Pi=\theta} \phi d\Pi}{A \oint_{\Pi=\theta} \Pi d\theta} \quad (28)$$

where $\Pi = p^\kappa$ ($\kappa = R/C_p$), and the symbols “ $\Pi \rightleftharpoons \lambda$ ” and “ $\Pi \rightleftharpoons \theta$ ” indicate that the contour integrations are to be carried out, using the finite-volume integration method described in

L97, in the (Π, λ) and (Π, θ) space, respectively.

Mass fluxes (x^*, y^*) and the winds (u^*, v^*) on the C-grid are accumulated for the large-time-step transport of tracer species (including water vapor) q .

$$q^{n+1} = \frac{1}{\delta p^{n+1}} [q^n \delta p^n + F(X^*, \Delta t, q^\theta) + G(Y^*, \Delta t, q^\lambda)] \quad (29)$$

where the time-accumulated mass fluxes (X^*, Y^*) are computed as

$$X^* = \sum_{i=1}^m x_i^*(u_i^*, \Delta\tau, \delta p_i^\theta), \quad Y^* = \sum_{i=1}^m y_i^*(v_i^*, \Delta\tau, \delta p_i^\lambda) \quad (30)$$

The time-averaged winds (U^*, V^*) , to be used as input for the computations of q^λ and q^θ , are defined as follows.

$$U^* = \frac{1}{m} \sum_{i=1}^m u_i^*, \quad V^* = \frac{1}{m} \sum_{i=1}^m v_i^* \quad (31)$$

To complete one full time step, Eq. (24)-(27), together with their counterparts on the C-grid are cycled m times using the fractional time step $\Delta\tau$, which are followed by the tracer transport using Eq. (19) with the large-time-step Δt . The use of the time accumulated mass fluxes and the time-averaged winds for the large-time-step tracer transport ensures the conservation of the tracer mass and maintains the highest degree of consistency possible under the time split integration procedure.

There is formally no Courant number related time step restriction associated with the transport processes. There is, however, a stability condition imposed by the gravity-wave processes. For application on the whole sphere, it is computationally advantageous to apply a high-latitude zonal filter to allow a dramatic increase of the size of the small time step $\Delta\tau$. The effect of the zonal filter is to stabilize the short-in-wavelength (and high-in-frequency) gravity waves that are being unnecessarily and unidirectionally resolved at very high latitudes in the zonal direction. To minimize the impact to meteorologically significant larger scale waves, the zonal filter is highly scale selective and is applied only to the diagnostic variables

on the auxiliary C-grid and the tendency terms in the D-grid momentum equations. No zonal filter is applied directly to any of the prognostic variables. Due to the two-grid approach and the stability of the FFSL transport scheme, the maximum size of the small-time-step is about two to three times larger than a model based on Arakawa and Lamb’s scheme on the C-grid. It is possible to avoid the use of the zonal filter if, for example, the “Cubed Sphere grid” (Sadourny 1972; Ronchi et al. 1996) is chosen. However, this would require a significant rewrite of the model codes including physics parameterizations, the land model, and most of the post processing packages.

The size of the small-time-step for the Lagrangian dynamics is only a function of the horizontal resolution. Applying the zonal filter, for the 2-degree horizontal resolution, a small-time-step size of 450 seconds can be used for the Lagrangian dynamics. From the large-time-step transport perspective, the small-time-step integration of the 2D Lagrangian dynamics can be regarded as a very accurate iterative solver, with m iterations, for computing the time mean winds and the mass fluxes, analogous in functionality to a semi-implicit algorithm’s elliptic solver (*e.g.*, Ringler et al. 2000). Besides accuracy, the merit of “explicit” versus “semi-implicit” algorithm ultimately depends on the computational efficiency of each approach. In light of the advantage of the explicit algorithm in parallelization, we do not regard the explicit algorithm for the Lagrangian dynamics as an impedance to computational efficiency.

4. A mass, momentum, and total energy conserving remapping algorithm

The Lagrangian surfaces that vertically bound the finite-volumes will eventually deform, particularly in the presence of persistent diabatic heating/cooling, in time scale of a few hours to a day depending on the strength of the heating and cooling, to a degree that it will negatively impact the accuracy of the horizontal-to-Lagrangian-surface transport and the computation of the pressure gradient terms. Therefore, a key to the success of the Lagrangian

control-volume discretization is an accurate and conservative algorithm for remapping the deformed Lagrangian coordinate back to a fixed Eulerian coordinate.

There are some degrees of freedom in the design of the remapping algorithm. To ensure conservation, the remapping algorithm is based on the reconstruction of the zonal and meridional “winds”, “tracer mixing ratios”, and “total energy” (volume integrated sum of the internal, potential, and kinetic energy), using the monotonic Piecewise Parabolic subgrid distributions with the hydrostatic pressure as defined by Eq. (23) as the remapping coordinate. We outline the remapping procedure as follows.

Step-1: Define a suitable Eulerian reference coordinate. The surface pressure typically plays an “anchoring” role in defining the terrain following Eulerian vertical coordinate. The mass in each layer (δp) is then computed according to the chosen Eulerian coordinate.

Step-2: Construct vertical subgrid profiles of tracer mixing ratios (q), zonal and meridional winds (u, v), and total energy (Γ) in the Lagrangian control-volume coordinate based on the Piece-wise Parabolic Method. The total energy Γ is computed as the sum of the finite-volume integrated geopotential ϕ , internal energy ($C_v T$), and the kinetic energy (K).

$$\Gamma = \frac{1}{\delta p} \int \left[C_v T + \phi + \frac{1}{2} (u^2 + v^2) \right] dp \quad (32)$$

Applying integration by parts and the ideal gas law, the above integral can be carried out as

$$\Gamma = C_p \bar{T} + \frac{1}{\delta p} \delta (p\phi) + K \quad (33)$$

where \bar{T} is the layer mean temperature, K is the kinetic energy, p is the pressure at layer edges, and C_v and C_p are the specific heat of the air at

constant volume and at constant pressure, respectively. Layer mean values of $[q, (u, v), \text{ and } \Gamma]$ in the Eulerian coordinate system are obtained by integrating analytically the sub-grid distributions, in the vertical direction, from model top to the surface, layer by layer. Since the hydrostatic pressure is chosen as the remapping coordinate, air and tracer mass, momentum, and total energy are conserved.

To convert the potential temperature Θ to the layer mean temperature the conversion factor is obtained by equating the following two equivalent forms of the hydrostatic relation.

$$\delta\phi = -C_p\Theta\delta\Pi \quad (34)$$

$$\delta\phi = -R\bar{T}\delta\ln p \quad (35)$$

where $\Pi = p^\kappa$. The conversion formula between layer mean temperature and layer mean potential temperature is

$$\Theta = \kappa \frac{\delta\ln p}{\delta\Pi} \bar{T} \quad (36)$$

Step-3: Compute kinetic energy in the Eulerian coordinate system for each layer. Substituting kinetic energy and the hydrostatic relationship Eq. (35) into (33), the layer mean temperature for *layer* $-k$ in the Eulerian coordinate is then retrieved from the reconstructed total energy (done in Step-2) by a fully explicit integration procedure starting from the surface up to the model top as follows:

$$\overline{T}_k = \frac{\Gamma_k - K_k - \phi_{k+\frac{1}{2}}}{C_p \left[1 - \kappa p_{k-\frac{1}{2}} \frac{\ln p_{k+\frac{1}{2}} - \ln p_{k-\frac{1}{2}}}{p_{k+\frac{1}{2}} - p_{k-\frac{1}{2}}} \right]} \quad (37)$$

The physical implication of retrieving the layer mean temperature from the total energy is that the dissipated kinetic energy, if any, is locally converted into internal energy via the vertically sub-grid mixing (dissipation) processes. Due to the monotonicity preserving nature of the sub-grid reconstruction the column-integrated kinetic energy inevitably decreases (dissipates), which leads to local frictional heating. The frictional heating is a physical process that maintains the conservation of the total energy in a closed system.

As viewed by an observer riding on the Lagrangian surfaces, the remapping procedure essentially performs the physical function of the relative-to-the-Eulerian-coordinate vertical transport, by vertically redistributing mass, momentum, and total energy from the Lagrangian control-volume back to the Eulerian framework. The remapping time step can be much larger than that used for the large-time-step tracer transport. In tests using the Held-Suarez forcing, a three-hour remapping time interval is found to be adequate. In the full model integration, one may choose the same time step used for the physical parameterizations so as to ensure the input to physical parameterizations are in the usual “Eulerian” vertical coordinate.

5. Idealized tests

We present results from two types of idealized tests. The first is a deterministic initial-value-problem test case illustrating the growth and propagation of baroclinic instability initiated by a localized perturbation. The second is the “climate” simulation using the Held-Suarez forcing. For both tests we used a 32-level hybrid $\sigma - p$ vertical coordinate as the “Eulerian” coordinate for the remapping procedure. Below 500 mb, this 32-level setup is the same as the NCAR CCM3’s 18-level setup for climate simulations (Kiehl, *et al.* 1996). To better

resolve the stratosphere, the vertical resolution is substantially increased (as compared to CCM3) near and above the tropopause level. The model top is located at 0.4 mb.

The initial condition for the baroclinic instability test case is specified analytically as

$$U(\theta, p) = U_o z e^{-\frac{z^2}{4}} \sin^4(2\theta), \quad (38)$$

where $z = \log\left(\frac{p_o}{p}\right)$, $P_o = 1000\text{ (mb)}$, $U_o = 35\text{ m/s}$. The mean flow, which is symmetric with respect to the equator, is in hydrostatic equilibrium with the meridional wind being identically zero. The balanced zonal mean temperature is then computed numerically. The base state thus constructed is a steady state solution to the 3D governing equations. To break the symmetry and to trigger the growth of the baroclinic instability, a localized initial temperature perturbation centered at 45N and 90E is superimposed to the mean field. Previous theoretical studies (*e.g.*, Lin and Pierrehumbert 1993) indicated that the localized disturbance will propagate eastward while growing exponentially. Due to nonlinearity and periodicity of the spherical geometry, the instability will saturate and the perturbation will cycle zonally to become a global mode.

Figure 1 depicted the prescribed zonal mean wind and the derived balanced temperature. The wind is a fairly realistic representation of the annual mean condition with the derived temperature showing a cold tropical tropopause centered near 100 mb and with realistic lapse rates throughout the globe. Experiments were carried out using three progressively higher horizontal resolutions: one at $2^\circ \times 2.5^\circ$ (denoted as B32), the second at $1^\circ \times 1.25^\circ$ (denoted as C32), and the third at $0.5^\circ \times 0.625^\circ$ (denoted as D32), with small-time-step of 450 seconds, 225 seconds, and 112.5 seconds, respectively. The remapping time step is fixed to be one hour for all presented tests.

Figure 2 compares, at day 10, the surface pressure perturbations and the temperature at the model's lowest layer. It is seen that the phases of the propagation of the disturbances agree remarkably well among all three resolutions. However, the amplitudes in the lower resolution runs are somewhat weaker. These are expected characteristics of the monotonicity-

preserving finite-volume algorithms. The initial-value problem tests provided no proof that the simulations are “correct” or have converged. In fact, the results show that even at approximately 55 km resolution the detailed features of the cyclones may still be under-resolved. Nevertheless, a reasonable degree of convergence, particularly the large-scale features, has been achieved, and there is no pathological amplification of the numerical noise in any resolutions we tested. While a monotonicity-preserving algorithm is beneficial to scalar transport, its advantage is unclear in climate simulations in which the preservation of variances is regarded as more important. This issue is examined using the Held-Suarez forcing.

We applied the same initial condition used in the above tests to initialize the Held-Suarez test. The integrations were carried out for more than four years. Statistics were computed only for the last 1000 days. Figure 3 and figure 4 show, respectively, for the B32 and C32 resolutions, the zonal mean u-wind, v-wind, temperature, and the vertical pressure velocity.

Within the Lagrangian framework, the vertical pressure velocity is diagnosed as follows.

$$\frac{dp_k}{dt} = \frac{p_k^{t+\Delta t} - p_k^t}{\Delta t}$$

where the subscript k indicates the k^{th} Lagrangian surface. $p_k^{t+\Delta t}$ is the pressure of the k^{th} Lagrangian surface at time $t + \Delta t$ before remapping (Lagrangian coordinate), p_k^t is the value at time t immediately after the previous remapping (Eulerian coordinate), and Δt is the remapping time step.

The simulated zonal mean fields are in good agreement with Held and Suarez’s results. In particular, there is a distinct “tropical tropopause” of about 190 degree Kelvin, and there is also a cold surface layer. The simulated zonal mean flows are not exactly symmetric with respect to the equator due to the asymmetric initial perturbation and the limited averaging period. There are subtle differences between the two resolutions. Most notably the “tropical tropopause” in the higher C32 resolution is a bit colder than that from the B32 case whereas the polar “tropopause” (not clearly defined, but roughly at 250 mb level) in the C32 is slightly warmer. The warming of the polar tropopause with increasing horizontal resolution

is consistent with full physics simulations using the CCM3 parameterizations (to be presented elsewhere).

Figure 5 (for B32 case) and figure 6 (for C32 case) show the eddy momentum transport, eddy heat transport, zonal wind variance, and the temperature variance. Except for the zonal wind variance, a good degree of convergence has been achieved between the two resolutions. However, the differences with Held-Suarez’s results were more pronounced in the second moment statistics. For example, the temperature variances in our simulations show only a single maxima in the upper troposphere of the midlatitudes whereas in the Held and Suarez’s results there is a secondary maxima, which could be of numerical origin.

To examine the impacts of monotonicity constraint, which damps strongly the two-grid-scale structures, to the simulated “climate”, we carried out another experiment with the B32 resolution but without applying the monotonicity constraint to all horizontal transport processes. Figure 7 and 8 show, respectively, the mean states and the eddy statistics. It is seen that without the monotonicity constraint the simulation is, not surprisingly, closer to the higher resolution (C32) case.

Figure 9 shows the differences in zonal mean temperature due to the monotonicity constraint. It indicates that, without the monotonicity constraint, poleward heat transport is more rigorous, resulting in warmer poles and cooler tropics. The monotonicity constraint’s seemingly negative impact to “climate simulations” needs to be re-examined in full model simulations, which is beyond the scope of this paper. It should be noted that the monotonicity constraint is highly desirable for the transport of water vapor, cloud water, and chemical tracers to prevent the generation of negative values. In short-term deterministic initial-value problems (*e.g.*, weather predictions), it can be argued that elimination of grid-scale numerical noise is more important than the maintenance of variances. On the other hand, it may be more important to preserve the variances in long-term climate simulations.

6. Concluding remarks

The finite-volume dynamical core described here has been successfully implemented into two general circulation modeling systems, the NASA/NCAR general circulation model (fvGCM, to be described elsewhere) and the Community Atmosphere Model (CAM). It is also in the process of being implemented into Geophysical Fluid Dynamics Laboratory’s Flexible Modeling System (FMS) for climate applications. At the NASA Data Assimilation Office (DAO), we have already successfully integrated the fvGCM into a new generation of the data assimilation system: the finite-volume Data Assimilation System (fvDAS). Numerical weather prediction experiments using the fvGCM with initial conditions produced by fvDAS indicated there is significant improvement in the forecast skill over DAO’s previous operational system (GEOS-3 DAS).

There are still some aspects of the numerical formulation in this dynamical core that can be further improved. For example, the choice of the horizontal grid, the computational efficiency of the split-explicit time marching scheme, the application of the various monotonicity constraints, and how the conservation of total energy is achieved. The vertical Lagrangian discretization with the associated remapping conserves the total energy exactly. The only remaining issue regarding the conservation of the total energy is the use of the apparently “diffusive” monotonicity preserving transport scheme for the horizontal discretization.

The full impact of the non-linear diffusion associated with the monotonicity constraint is difficult to access. All discrete schemes must address the problem of subgrid-scale mixing. The non-linear diffusion in the finite-volume scheme creates strong local mixing when monotonicity principles are violated. However, this local mixing diminishes quickly as the resolution matches better to the spatial structure of the flow. In other numerical schemes, however, an explicit (and tunable) linear diffusion is often added to the equations to provide the subgrid-scale mixing as well as to smooth and/or stabilize the time marching.

To compensate for the loss of total energy due to horizontal discretization, one could apply a global fixer to add the loss in kinetic energy due to “diffusion” back to the thermodynamic

equation so that the total energy is conserved. However, our experience shows that even without the “energy fixer” the loss in total energy (in flux unit) in a full GCM simulation is less than $2 \text{ (} W/m^2 \text{)}$ with the 2 degrees resolution, and much smaller with higher resolutions. Alternatively, one could consider using the total energy as a prognostic variable so that the total energy could be automatically conserved.

Extension of the algorithms described in this paper to unstructured grids is possible but not straightforward. We are currently developing a high-order monotonicity preserving finite-volume transport scheme for the Geodesic grid, which is to be used in the future development of the finite-volume dynamical core, without the hydrostatic limitation.

Acknowledgements. The author is indebted to Drs. R. B. Rood and R. Atlas for their supports and encouragements during the development of the NASA finite-volume General Circulation Model. The author benefited greatly from discussions with B. van Leer and collaboration with NCAR scientists. Constructive criticisms from Drs. P. J. Rasch and B. A. Boville led to significant computational and algorithmic improvements. The author also thanks Dr. K.-S. Yeh and W. Putman for proof reading the manuscript.

Appendix-A: The governing equations for the hydrostatic atmosphere

For reference, we present the governing equations for the hydrostatic atmosphere on the sphere with a general vertical coordinate ζ (*e.g.*, Kasahara 1974). Using standard notations, the hydrostatic balance equation is:

$$\frac{1}{\rho} \frac{\partial p}{\partial \zeta} + g = 0 \quad (39)$$

where ρ is the density of the air, p the pressure, and g is the gravitational constant. Introducing the “*pseudo-density*” $\pi = \frac{\partial p}{\partial \zeta}$, vertical pressure gradient in the general coordinate, from the hydrostatic balance equation, the *pseudo-density* and the true density are related as follows:

$$\pi = -\frac{\partial \phi}{\partial \zeta} \rho \quad (40)$$

where $\phi = gz$ is the geopotential. Note that π reduces to the true density if $\zeta = -gz$, and the surface pressure P_s if $\zeta = \sigma$ ($\sigma = \frac{p}{P_s}$). The conservation of total air mass using π as the prognostic variable can be written as

$$\frac{\partial}{\partial t} \pi + \nabla \cdot (\vec{V} \pi) = 0 \quad (41)$$

where $\vec{V} = (u, v, \frac{d\zeta}{dt})$. Similarly, the mass conservation law for tracers (or water vapor) can be written as

$$\frac{\partial}{\partial t} (\pi q) + \nabla \cdot (\vec{V} \pi q) = 0, \quad (42)$$

where q is the mass mixing ratio (or specific humidity) of the tracers (or water vapor). Choosing the potential temperature Θ as the thermodynamic variable, the first law of thermodynamics can be formulated as

$$\frac{\partial}{\partial t}(\pi\Theta) + \nabla \cdot (\vec{V} \pi\Theta) = 0 \quad (43)$$

Let (λ, θ) denote the (longitude, latitude) coordinate, the momentum equations are written in the “vector-invariant form” (*e.g.*, Arakawa and Lamb 1981)

$$\frac{\partial}{\partial t}u = \Omega v - \frac{1}{A \cos \theta} \left[\frac{\partial}{\partial \lambda} (\kappa + \phi - \nu D) + \frac{1}{\rho} \frac{\partial}{\partial \lambda} p \right] - \frac{d\zeta}{dt} \frac{\partial u}{\partial \zeta} \quad (44)$$

$$\frac{\partial}{\partial t}v = -\Omega u - \frac{1}{A} \left[\frac{\partial}{\partial \theta} (\kappa + \phi - \nu D) + \frac{1}{\rho} \frac{\partial}{\partial \theta} p \right] - \frac{d\zeta}{dt} \frac{\partial v}{\partial \zeta} \quad (45)$$

where A is the radius of the earth, ν is the coefficient for the optional divergence damping, D is the horizontal divergence, Ω is the vertical component of the absolute vorticity, κ is the kinetic energy, ϕ is the geopotential, and ω is the angular velocity of the earth.

$$D = \frac{1}{A \cos \theta} \left[\frac{\partial}{\partial \lambda} (u) + \frac{\partial}{\partial \theta} (v \cos \theta) \right], \quad \kappa = \frac{1}{2} (u^2 + v^2),$$

$$\Omega = 2\omega \sin \theta + \frac{1}{A \cos \theta} \left[\frac{\partial}{\partial \lambda} v - \frac{\partial}{\partial \theta} (u \cos \theta) \right]$$

Note that the last term in Eq. (44) and (45) vanishes if ζ is a conservative quantity [*e.g.*, entropy under adiabatic condition (*e.g.*, Hsu and Arakawa 1990) or an imaginary conservative tracer (see section 3)], and the 3D divergence operator becomes 2D along constant ζ surfaces.

Appendix-B: Relaxed monotonicity constraints for PPM The original PPM as described by Colella and Woodward (1984) has been modified to improve its computational performance and to reduce the numerical diffusion. The PPM is built on the second order van Leer scheme. Given the cell-mean value q_i and assuming uniform grid spacing, the “mismatch” (Lin et al. 1994) of the piecewise linear distribution is determined as

$$\Delta q_i^{mono} = \text{sign} [\min(|\Delta q_i|, \Delta q_i^{min}, \Delta q_i^{max}), \Delta q_i] \quad (46)$$

where

$$\Delta q_i = \frac{1}{4} (q_{i+1} - q_{i-1})$$

$$\Delta q_i^{max} = \max(q_{i-1}, q_i, q_{i+1}) - q_i, \quad \Delta q_i^{min} = q_i - \min(q_{i-1}, q_i, q_{i+1})$$

In the above equations and the rest of the appendix the functions *sign*, *min*, and *max* are as defined in the Fortran language. To uniquely determine a parabolic polynomial within the finite-volume, in addition to the volume mean value, the values at both edges of the parabola must be determined. The first guess value at the left edge of the piecewise parabolic distribution is computed as

$$q_i^- = \frac{1}{2}(q_{i-1} + q_i) + \frac{1}{3}(\Delta q_{i-1}^{mono} - \Delta q_i^{mono}) \quad (47)$$

By continuity, the right edge value of cell (i) is simply the left-edge value of cell (i+1). That is, $q_i^+ = q_{i+1}^-$. The application of a monotonicity constraint breaks the continuity of the subgrid distribution between the cells. In the current implementation, different constraints are used in the horizontal and vertical directions. For the horizontal direction, the first guess edge values as computed by Eq. (47) are adjusted as follows.

$$q_i^- \leftarrow q_i - \text{sign} \left[\min(|2\Delta q_i^{mono}|, |q_i^- - q_i|), 2\Delta q_i^{mono} \right] \quad (48)$$

$$q_i^+ \leftarrow q_i + \text{sign} \left[\min(|2\Delta q_i^{mono}|, |q_i^+ - q_i|), 2\Delta q_i^{mono} \right] \quad (49)$$

The above constraint produces less diffusive results and is much simpler than the original PPM. To further reduce the implicit damping, an even less diffusive but more complicated quasi-monotonic constraint is used for the vertical remapping of the moisture and all tracers. The following constraint is based on the improved-wave-resolution scheme of Huynh (Huynh

1996).

Left (top) edge:

$$q_i^- \leftarrow \min [max(q_i^-, q_i^{min}), q_i^{max}] \quad (50)$$

where

$$q_i^{min} = \min (q_i, q_i^{mp}, q_i^{lc}) , \quad q_i^{max} = \max (q_i, q_i^{mp}, q_i^{lc})$$

$$q_i^{mp} = q_i - 2\Delta q_i^{mono} , \quad q_i^{lc} = q_i + \frac{3}{2}(\Delta q_{i+2}^{mono} - \Delta q_i^{mono}) - \Delta q_i^{mono}$$

Right (bottom) edge:

$$q_i^+ \leftarrow \min [max(q_i^+, q_i^{min}), q_i^{max}] \quad (51)$$

where

$$q_i^{min} = \min (q_i, q_i^{mp}, q_i^{lc}) , \quad q_i^{max} = \max (q_i, q_i^{mp}, q_i^{lc})$$

$$q_i^{mp} = q_i + 2\Delta q_i^{mono} , \quad q_i^{lc} = q_i + \frac{3}{2}(\Delta q_i^{mono} - \Delta q_{i-2}^{mono}) + \Delta q_i^{mono}$$

After the application of one of the constraints, the “curvature” of the parabola is computed using the mean and the two edge values as

$$q_i'' = 6 \left[q_i - \frac{1}{2}(q_i^- + q_i^+) \right] \quad (52)$$

References

- Allen, D. J., P. J. Kasibhatla, A. M. Thompson, R. B. Rood, B. G. Doddridge, K. E. Pickering, R. D. Hudson, and S.-J. Lin, 1996: Transport induced interannual variability of carbon monoxide determined using a chemistry and transport model. *J. Geophys. Res.*, **101**, 28655-28669.
- Arakawa, A and V. R. Lamb, 1981: A potential enstrophy and energy conserving scheme for the shallow-water equations. *Mon. Wea. Rev.*, **109**, 18-36.
- Bourke, W., 1974: A multilevel spectral model. I. Formulation and hemispheric integration. *Mon. Wea. Rev.*, **102**, 687-701.
- Carpenter, R. L., K. K. Droegemeier, P. R. Woodward, and C. E. Hane, 1990: Application of the piecewise parabolic method to meteorological modelling. *Mon. Wea. Rev.*, **118**, 586-612.
- Chin, M., R. B. Rood, S.-J. Lin, J.-F. Muller, and A. M. Thompson, 2000: Atmospheric sulfur cycle simulation in the global model GOCART: Model description and global properties. *J. Geophys. Res.*, **105**, 24, 671-24, 687.
- Colella, P., and P. R. Woodward, 1984: The piecewise parabolic method (PPM) for gas-dynamical simulations. *J. Comput. Phys.*, **54**, 174-201.
- Harten A., 1989: ENO schemes with subcell resolution. *J. Comput. Phys.*, **83**, 148.
- Held, I. M., and M. J. Suarez, 1994: A proposal for the intercomparison of the dynamical cores of atmospheric general circulation models. *Bull. Amer. Meteor.*, **73**, 1825-1830.
- Hsu, Y.-J. G., and A. Arakawa, 1990: Numerical modeling of the atmosphere with an isentropic vertical coordinate. *Mon. Wea. Rev.*, **118**, 1933-1959.
- Huynh, H. T., 1996: Schemes and constraints for advection. *Fifth international conference on numerical methods in fluid dynamics, Monterey*, June 24-28, 1996, CA, USA.
- Kasahara, A., 1974: Various vertical coordinate systems used for numerical weather prediction. *Mon. Wea. Rev.*, **102**, 504-522.
- Kiehl, J. T., J. J. Hack, G. B. Bonan, B. A. Boville, B. P. Briegleb, D. L. Williamson, and P. J. Rasch 1996: Description of the NCAR Community Climate Model (CCM3). *NCAR*

Technical Note, NCAR/TN-420+STR, Boulder, CO, 152pp.

Leveque, R. J., 2002: Finite volume methods for hyperbolic problems. *Cambridge university press*, 558pp.

Lin, S.-J., and R. T. Pierrehumbert, 1993: Is the mid-latitude zonal flow absolutely unstable? *J. Atmos. Sci.*, **51**, 1282-1297.

Lin, S.-J., W. C. Chao, Y. C. Sud, and G. K. Walker, 1994: A class of the van Leer-type transport schemes and its applications to the moisture transport in a general circulation model. *Mon. Wea. Rev.*, **122**, 1575-1593.

Lin, S.-J., and R. B. Rood, 1996: Multidimensional Flux Form Semi-Lagrangian Transport schemes. *Mon. Wea. Rev.*, **124**, 2046-2070.

Lin, S.-J., 1997: A finite-volume integration method for computing pressure gradient forces in general vertical coordinates. *Q. J. Roy. Met. Soc.*, **123**, 1749-1762.

Lin, S.-J., and R. B. Rood, 1997: An explicit flux-form semi-Lagrangian shallow water model on the sphere. *Q. J. Roy. Met. Soc.*, **123**, 2531-2533.

Lin, S.-J., 1998: Reply to comments by T. Janjic on "A finite-volume integration method for computing pressure gradient forces in general terrain-following coordinates". *Q. J. Roy. Met. Soc.*, **124**, 1749-1762.

Lin, S.-J., and R. B. Rood, 1998: A flux-form semi-Lagrangian general circulation model with a Lagrangian control-volume vertical coordinate. *The Rossby-100 symposium, Stockholm, Sweden*.

Lin, S.-J., and R. B. Rood, 1999: Development of the joint NASA/NCAR General Circulation Mode. *Preprint, 13th conference on Numerical Weather Prediction*, Denver, CO.

Machenhauer, B., and M. Olk, 1996: On the development of a cell-integrated semi-Lagrangian shallow water model on the sphere. *Proceedings of ECMWF workshop on semi-Lagrangian methods*, 6-8, Nov. 1995.

Randall, D. A., 1994: Geostrophic adjustment and the finite-difference shallow-water equations. *Mon. Wea. Rev.*, **122**, 1371-1377.

- Ringler, T. D., R. P. Heikes, and D. A. Randall, 2000: Modeling the atmospheric general circulation using a spherical geodesic grid: A new class of dynamical cores. *Mon. Wea. Rev.*, **128**, 2471-2490.
- Roe, P. L., 1981: Approximate Riemann solvers, parameter vectors, and difference schemes. *J. Comput. Phys.*, **43**, 357.
- Ronchi, C., R. Iacono, and P. S. Paolucci, 1996: The "Cubed Sphere": A new method for the solution of partial differential equations in spherical geometry. *J. Comput. Phys.*, **124**, 93-114.
- Rood, R. B., 1987: Numerical advection algorithms and their role in atmospheric transport and chemistry models. *Rev. Geophys.*, **25**, 71-100.
- Rotman, D., J. Tannahill, D. Kinnison, P. Connell, Bergmann, Proctor, J. Rodriguez, S.-J. Lin, R. B. Rood, M. Prather, P. Rasch, D. Considine, R. Ramaroson, R. Kawa, 2001: Global Modeling Initiative Assessment Model: Model description, integration and testing of the transport shell. *J. Geophys. Res.*, Vol. **106**, No. D2, 1669-1691.
- Sadourny, R., 1972: Conservative finite-difference approximations of the primitive equations on quasi-uniform spherical grids. *Mon. Wea. Rev.*, **100**, 136-144.
- Shu, C.-W., and S. Osher, 1988: Efficient implementation of essentially non-oscillatory schemes. *J. Comput. Phys.*, **77**, 439.
- Starr, V. P., 1945: A quasi-Lagrangian system of hydrodynamical equations. *J. Meteor.*, **2**, 227-237.
- Thuburn, J., 1996: Multidimensional flux-limited advection schemes. *J. Comput. Phys.*, **123**, 74-83.
- Van Leer, B., 1977: Toward the ultimate conservative difference scheme. Part IV: A new approach to numerical convection. *J. Comput. Phys.*, **23**, 276-299.
- Woodward, P. R., and P. Colella, 1984: The numerical simulation of two-dimensional fluid flow with strong shocks. *J. Comput. Phys.*, **54**, 115-173.

List of Figures:

Figure 1. Zonal mean wind and the derived balanced temperature.

Figure 2. The surface pressure perturbation and the temperature at the lowest model layer at day-10 for three different horizontal resolutions.

Figure 3. The 1000-day average of zonal mean wind (upper left panel), meridional wind (upper right panel), temperature (lower left panel), and vertical pressure velocity (lower right panel) simulated with the Held-Suarez forcing at the 2x2.5 degrees resolution (B32).

Figure 4. As in figure 3, but for the 1x1.25 degrees resolution (C32).

Figure 5. The 1000-day average of eddy statistics: eddy momentum transport (upper left panel), heat transport (upper right panel), zonal wind variance (lower left panel), and temperature variance (lower right panel) simulated with the Held-Suarez forcing at the 2x2.5 degrees resolution (B32).

Figure 6. As in figure 5, but for the 1x1.25 degrees resolution (C32).

Figure 7. As in Figure 3 (B32 resolution), but without the application of the monotonicity constraint.

Figure 8. As in Figure 5 (B32 resolution), but without the application of the monotonicity constraint.

Figure 9. Temperature differences due to the application of the monotonicity constraint.

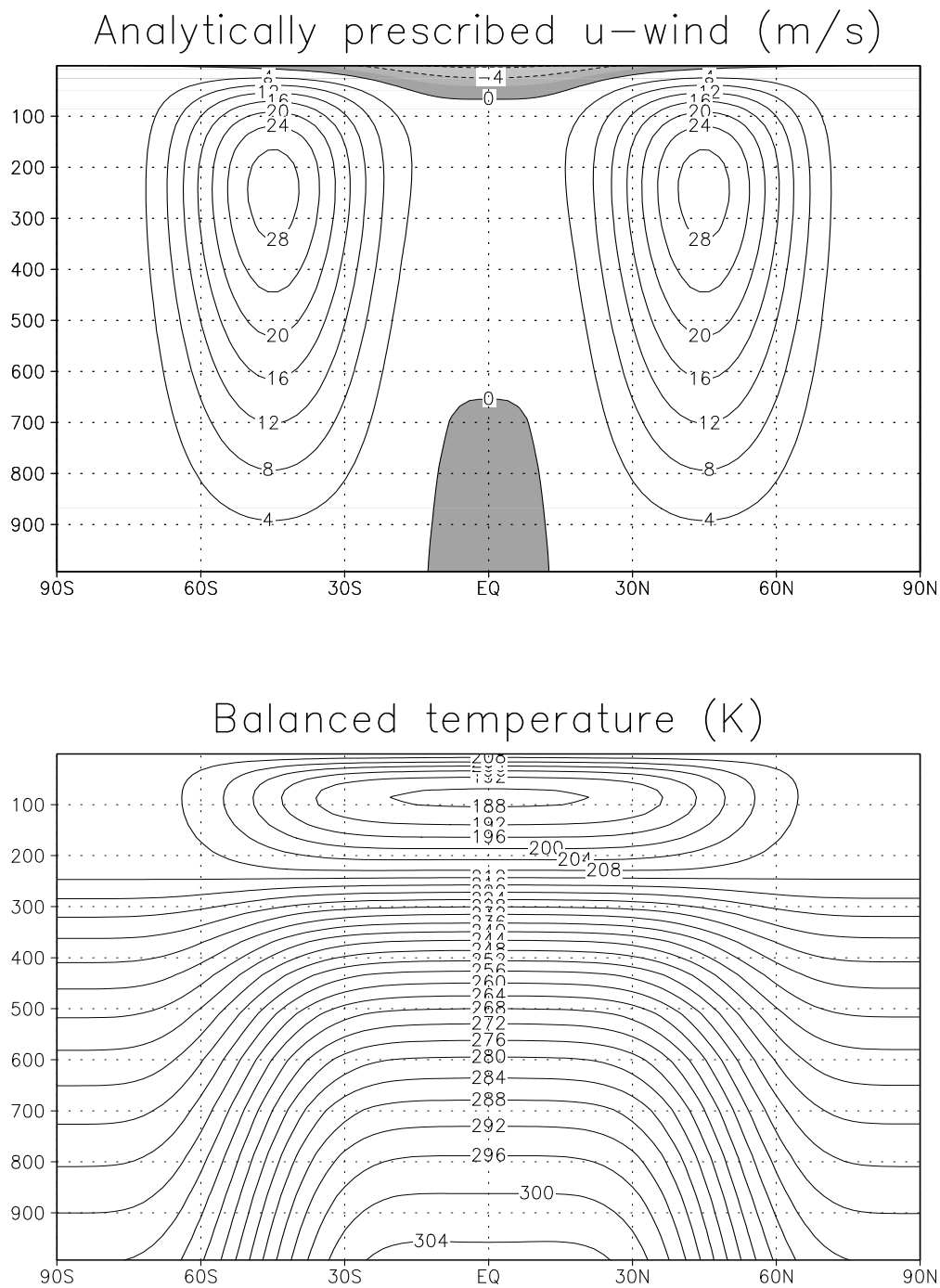


Figure 1. Zonal mean wind and the derived balanced temperature.

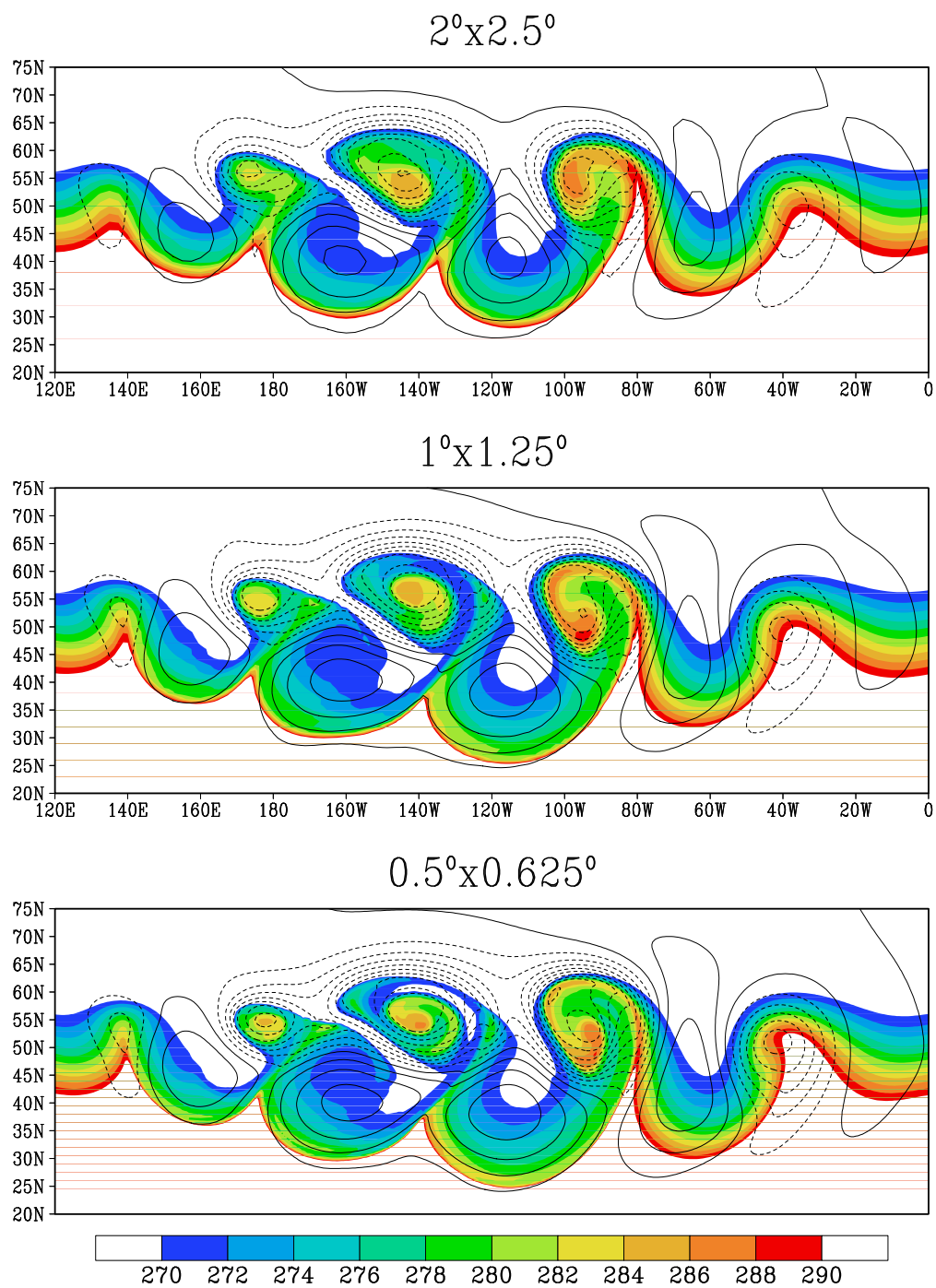


Figure 2. The surface pressure perturbation and the temperature at the lowest model layer at day-10 for three different horizontal resolutions.

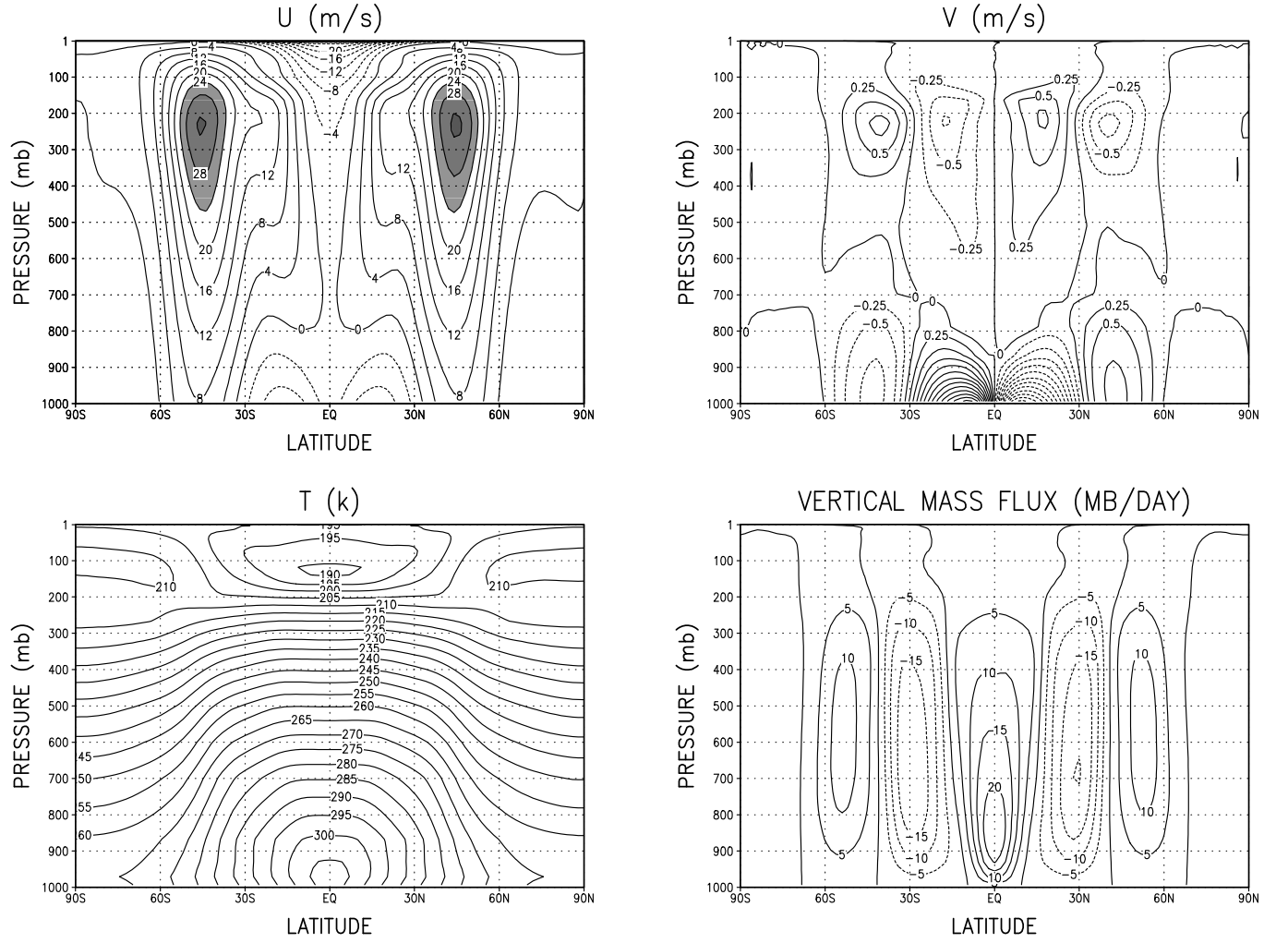


Figure 3. The 1000-day average of zonal mean wind (upper left panel), meridional wind (upper right panel), temperature (lower left panel), and vertical pressure velocity (lower right panel) simulated with the Held-Suarez forcing at the 2×2.5 degrees resolution (B32).

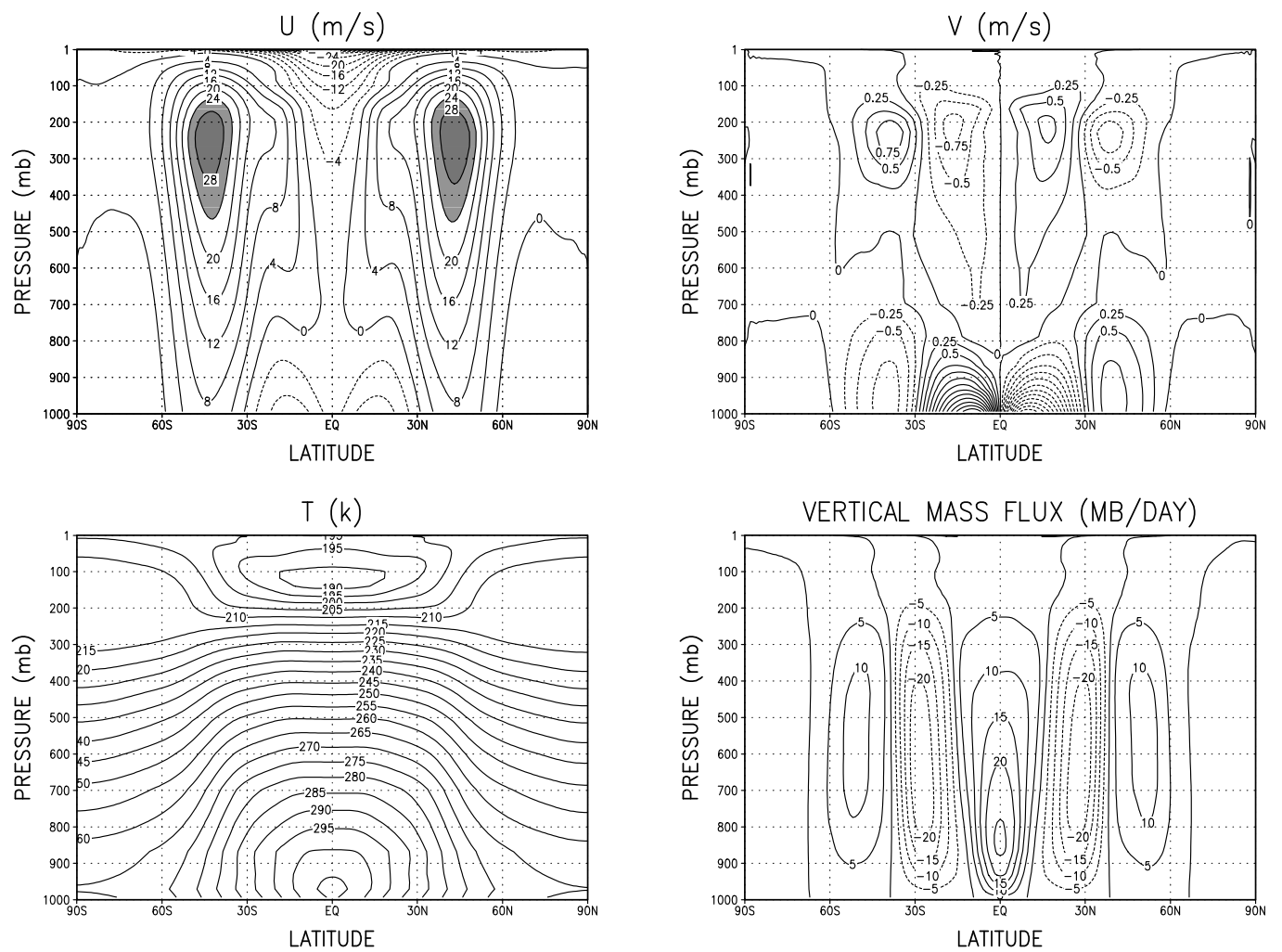


Figure 4. As in figure 3, but for the 1x1.25 degrees resolution (C32).

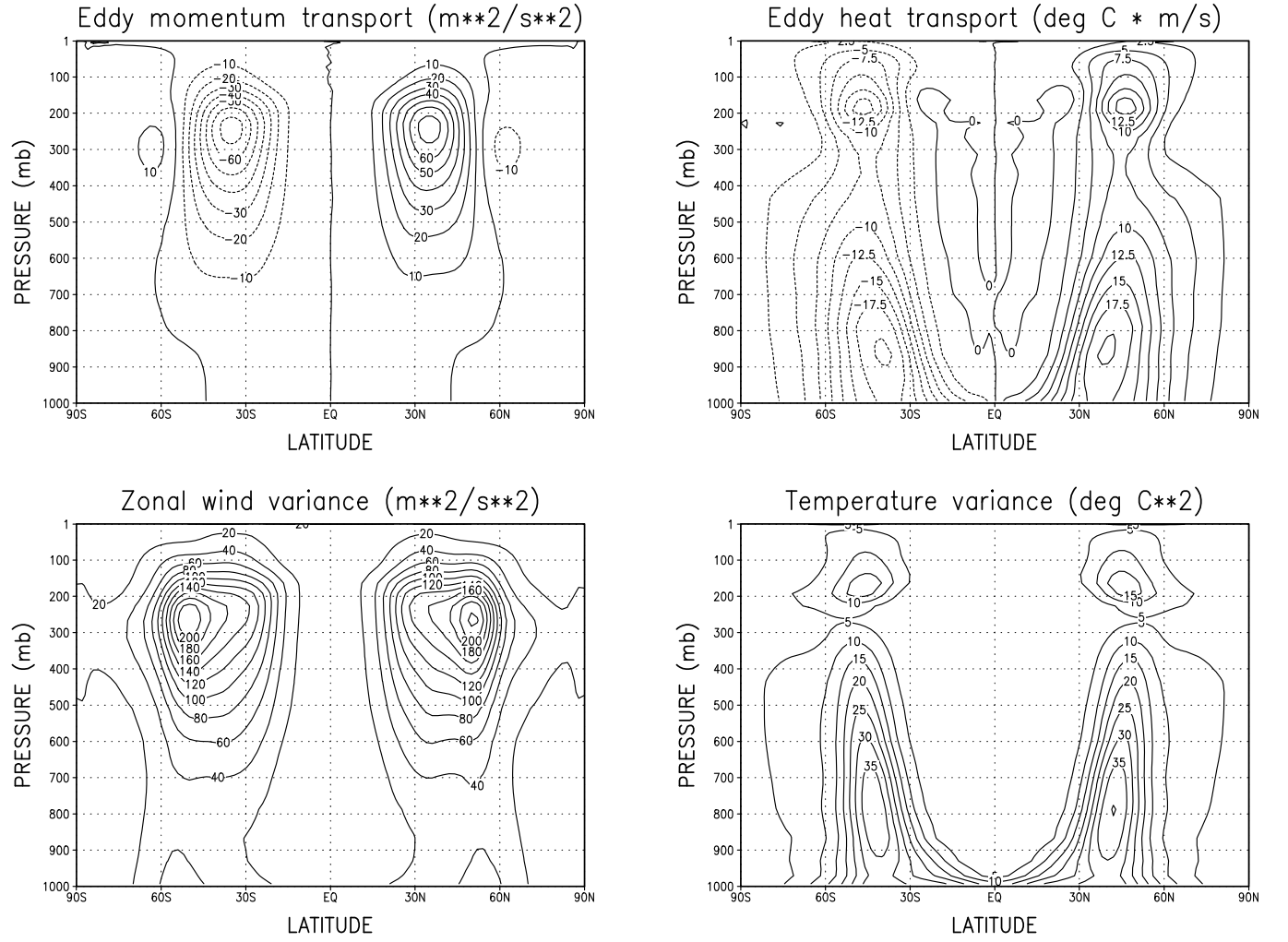


Figure 5. The 1000-day average of eddy statistics: eddy momentum transport (upper left panel), heat transport (upper right panel), zonal wind variance (lower left panel), and temperature variance (lower right panel) simulated with the Held-Suarez forcing at the 2×2.5 degrees resolution (B32).

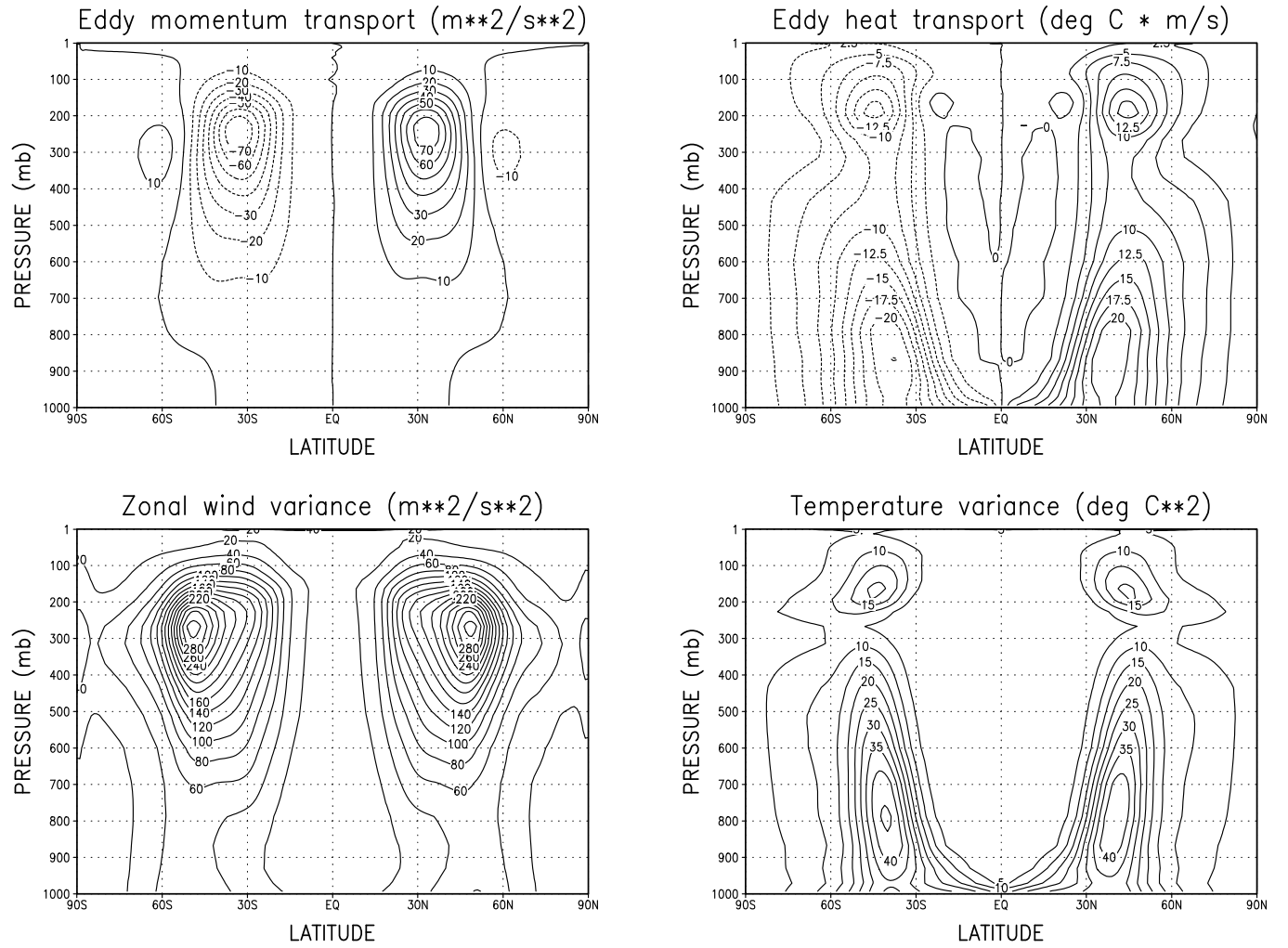


Figure 6. As in figure 5, but for the 1x1.25 degrees resolution (C32).

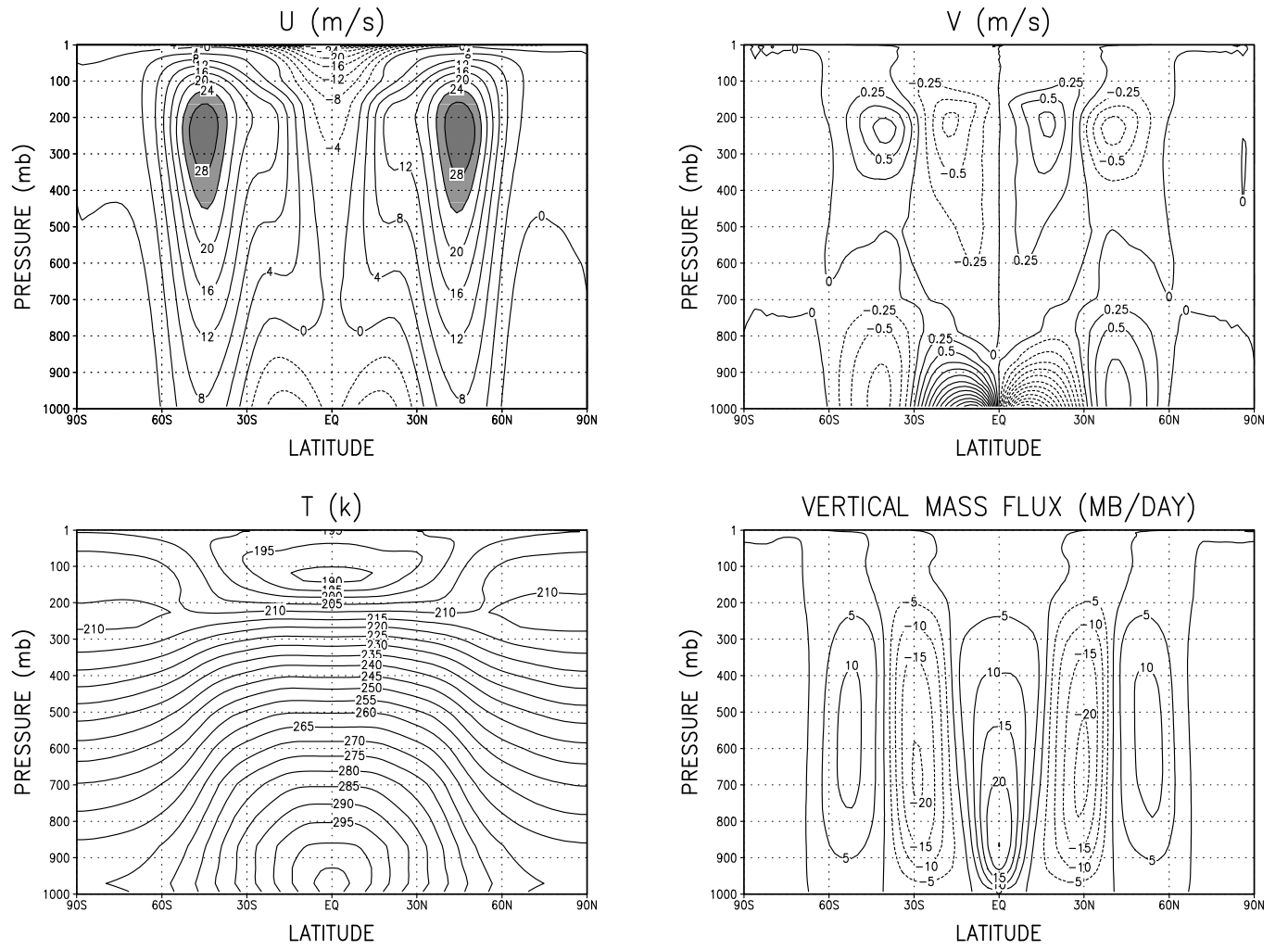


Figure 7. As in Figure 3 (B32 resolution), but without the application of the monotonicity constraint.

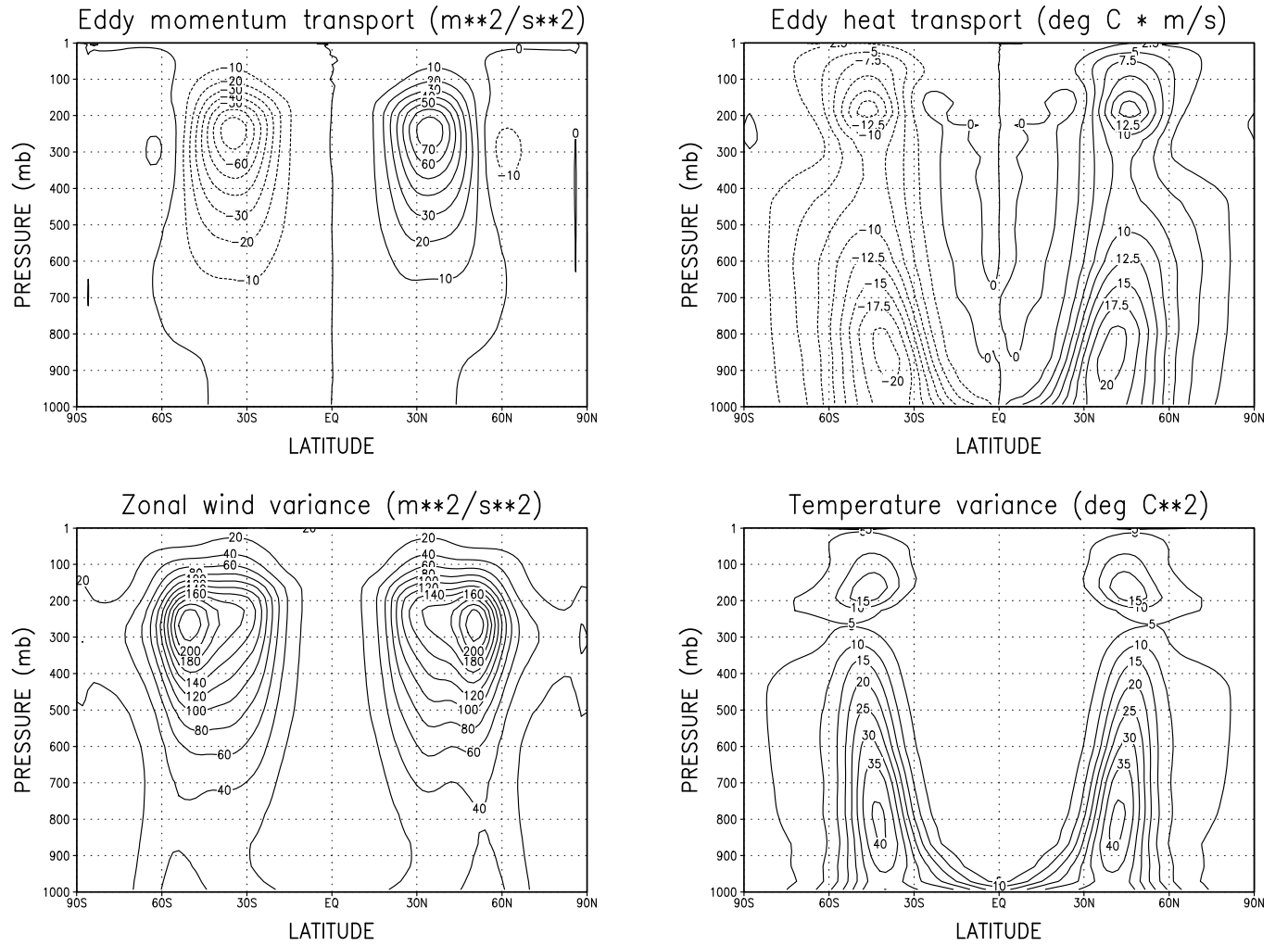


Figure 8. As in Figure 5 (B32 resolution), but without the application of the monotonicity constraint.

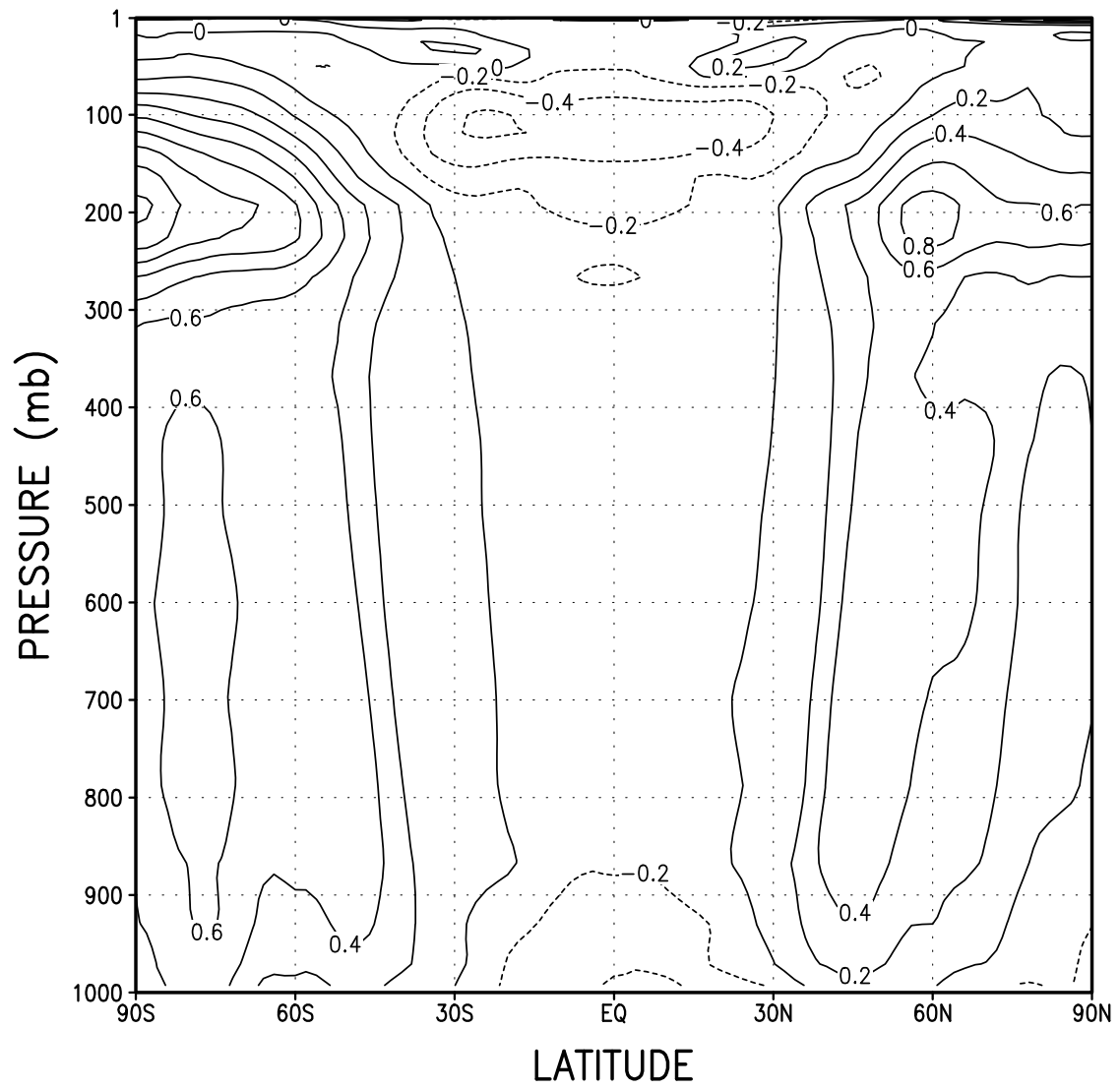


Figure 9. Temperature differences due to the application of the monotonicity constraint.